

# Environmental Science Advances

Accepted Manuscript

This article can be cited before page numbers have been issued, to do this please use: R. ZHANG, Z. WANG, K. T. M. Ho, N. Graham, A. Tan and P. Lee, *Environ. Sci.: Adv.*, 2026, DOI: 10.1039/D5VA00420A.



This is an Accepted Manuscript, which has been through the Royal Society of Chemistry peer review process and has been accepted for publication.

Accepted Manuscripts are published online shortly after acceptance, before technical editing, formatting and proof reading. Using this free service, authors can make their results available to the community, in citable form, before we publish the edited article. We will replace this Accepted Manuscript with the edited and formatted Advance Article as soon as it is available.

You can find more information about Accepted Manuscripts in the [Information for Authors](#).

Please note that technical editing may introduce minor changes to the text and/or graphics, which may alter content. The journal's standard [Terms & Conditions](#) and the [Ethical guidelines](#) still apply. In no event shall the Royal Society of Chemistry be held responsible for any errors or omissions in this Accepted Manuscript or any consequences arising from the use of any information it contains.

## Environmental Significance Statement

View Article Online  
DOI: 10.1039/D5VA00420A

Methane is a double-edged molecule—an important renewable energy source yet a potent greenhouse gas. This study elucidates a previously unclear abiotic and biotic mechanism of reactive oxygen species (ROS)–driven methane formation, revealing how cellular redox reactions involving  $\text{Fe}^{3+}$ , ascorbic acid, and methylated compounds can generate methane even in oxygenated environments. By integrating quantum (Harrow–Hassidim–Lloyd) and classical (Levenberg–Marquardt) microkinetic simulations, we quantify key rate constants and demonstrate that ferryl ion reactions, rather than hydroxyl radicals, dominate ROS-mediated methane production. These insights advance understanding of methane cycling in both engineered and natural systems, offering new directions for optimising micro-aerated anaerobic digestion and predicting methane emissions from oxygen-exposed ecosystems under changing redox and oxygen conditions.



View Article Online  
DOI: 10.1039/D5VA00420A

# *Microkinetic characterization of ROS-driven methane production through quantum and classical simulations*

Ronghan Zhang<sup>a,b,\*</sup>, Zexuan Wang<sup>a,b,\*</sup>, Kin Tung Michael Ho<sup>a</sup>, Nigel J.D. Graham<sup>a</sup>, Giin-Yu

Amy Tan<sup>b,\*\*</sup>, Po-Heng Henry Lee<sup>a,\*\*</sup>

<sup>a</sup> Department of Civil and Environmental Engineering, Imperial College London, London, SW7 2AZ, UK

<sup>b</sup> Department of Architecture and Civil Engineering, City University of Hong Kong, Hong Kong SAR, China

\* Co-first authors email address: rzhang343-c@my.cityu.edu.hk; zexuawang4-c@my.cityu.edu.hk

\*\* Co-corresponding author email address: amytan@cityu.edu.hk; [po-heng.lee@imperial.ac.uk](mailto:po-heng.lee@imperial.ac.uk)

## Abstract

Methane is ubiquitous in natural and engineered settings, but the mechanisms of reactive oxygen species (ROS)-driven methane production in living organisms remain unclear. Unraveling the interactions and microkinetics among ROS, iron species, and organic methyl groups (MET) is crucial for reducing emissions and optimizing energy recovery. In this study, the quantum Harrow-Hassidim-Lloyd (HHL) algorithm and classical Levenberg-Marquardt (LM) algorithm were employed to: 1) investigate the primary pathway of Fe<sup>3+</sup> and ascorbic acid (ASC) reactions, 2) determine the kinetic parameters for the reaction between [Fe<sup>IV</sup>=O]<sup>2+</sup> and MET, and 3) simulate the ROS-driven methane production pathway under specific abiotic conditions. The results revealed



that  $\text{Fe}^{3+}$  and ASC are primarily responsible for the redox reaction, with a kinetic rate constant of  $1.83 \times 10^{-4} \text{ M}^{-1}\text{s}^{-1}$  for the reaction between  $[\text{Fe}^{\text{IV}}=\text{O}]^{2+}$  and MET, and a  $\sim 10\%$  conversion rate of MET to methane. Our study establishes a theoretical framework for ROS-driven methane production. While identifying a feasible pathway for engineered and natural systems, further investigation and validation are needed to quantify its specific contribution in complex environments. Furthermore, this work demonstrates the potential of hybrid quantum-classical simulations for microkinetic analysis.

**Keywords:** Reactive oxygen species (ROS), Methane production, Fenton reaction, Microkinetic modeling, Quantum algorithm.

## 1. Introduction

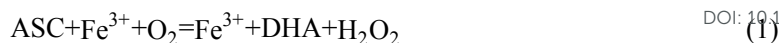
As global warming intensifies, it is of great significance to develop clean energy that can replace fossil fuel energy. <sup>1</sup> Methane is a renewable, clean energy source, albeit also a potent greenhouse gas. Harnessing methane production and collection for energy purposes presents a promising approach to mitigate greenhouse gas emissions. Methane production through anaerobic digestion (AD) can be enhanced by 10–30% using micro-aeration ( $2.63 - 37.5 \text{ mL O}_2 / \text{L}_R \cdot \text{d}$ , where  $\text{L}_R$  is the reactor working volume), which improves hydrolysis and generates reactive oxygen species (ROS) ( $0.27 - 0.29 \text{ mM H}_2\text{O}_2$  per cycle). <sup>2-8</sup> Contrary to popular belief that methane can only be produced under anaerobic conditions, enhanced methane formation has been observed in natural systems in the presence of oxygen, including oxygen-rich wetlands and oceans, where the addition of oxygen increased methane emissions by 4–10 fold. <sup>9,10</sup> The ability to produce methane appears to be deeply rooted in evolution and present in all living organisms. Through coupling oxygen-generated ROS



with methane production as part of an organism's innate oxidative stress mechanism, this mitigates ROS-induced oxidative damage. For example, *Bacillus subtilis* and *Escherichia coli* showed a 1.2–3.2 times methane yield increases in the presence of ROS as compared to that of non-ROS condition.<sup>3</sup> Leveraging on these emerging insights can provide new avenues for mitigating emissions and improving renewable energy harvesting. However, the precise mechanisms and micro-kinetics underlying the role of ROS in facilitating methane production remain poorly understood.

ROS-driven methane production has been linked to the presence of methyl group-containing organosulfur compounds, ROS, Fe<sup>2+</sup> and reducing agent ascorbic acid (ASC) (Figure 1a).<sup>3, 11</sup> Fe<sup>2+</sup> and H<sub>2</sub>O<sub>2</sub> (a form of ROS) can undergo Fenton reaction to generate Fe<sup>3+</sup>, hydroxyl radicals (•OH) and ferryl ions ([Fe(IV)=O]<sup>2+</sup>). [Fe(IV)=O]<sup>2+</sup> and •OH can react with methyl-containing organosulfur compounds to form methane.<sup>11</sup> The Fe<sup>3+</sup> produced can be reduced by ASC to regenerate Fe<sup>2+</sup>, sustaining the Fenton reaction. It is expected that these chemical species are present in natural and AD-engineered systems. Iron, an active metal predominantly coordinated in heme groups and iron-sulfur clusters that drive electron transport chains and participates in redox reactions, is widely present in living organisms including microorganisms.<sup>12</sup> Exposure of microbes to oxygen often produces ROS, which damage cellular structures and impair metabolisms.<sup>13</sup> ASC may play a crucial role in cellular protective mechanisms from ROS damage by facilitating iron and ROS redox reactions, thereby producing methane as a byproduct. However, there is a discrepancy in the proposed mechanisms for the interaction between ASC and iron species (Figure 1b). Here, two competing mechanisms are possible: a catalytic mechanism proposed by Buettner (Eq. 1) and a redox mechanism proposed by Buettner and Jurkiewicz (Eq. 2),<sup>14, 15</sup> as shown below:





- where DHA is dehydroascorbic acid



- where  $\text{A}^{\cdot-}$  is the ascorbate radical

Models proposed by Shen et al. showed that the catalysis degree of the reaction was 4 to 6-fold greater than that of the redox reaction.<sup>16</sup> However, experimental data from Elmagirbi et al. indicated that 76% of  $\text{Fe}^{3+}$  was converted to  $\text{Fe}^{2+}$  in the presence of ASC, suggesting that only 24% of  $\text{Fe}^{3+}$  may participate in the catalyst reaction.<sup>17</sup> Currently, it is unclear which pathway, whether redox or catalysis, plays a more significant role in promoting ROS-activated microkinetics. If the redox reaction between ASC and  $\text{Fe}^{3+}$  dominates, it can produce  $\text{Fe}^{2+}$  which promotes the ROS-driven methane production pathway to mitigate oxidative cell damage. In contrast, if the catalytic reaction is dominant, it will produce additional  $\text{H}_2\text{O}_2$ , which can cause cell damage and inhibit the methane production pathway.



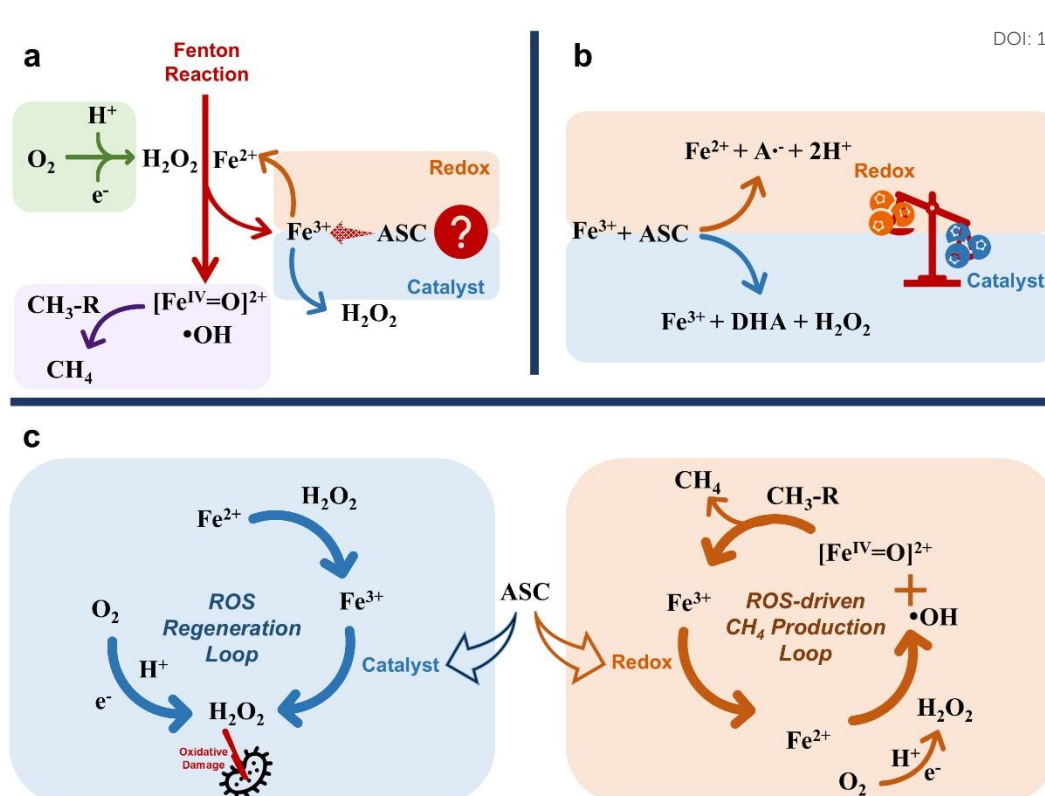


**Figure 1.** Proposed reaction pathways of the ROS-driven methane production loop: (a) the chemical processes involved in the biological Fenton reaction; (b) the catalyst and redox reactions between ASC and  $Fe^{3+}$ ; (c) the two possible reaction loops: ROS regeneration loop and ROS-driven methane production loop.

Overall, the interaction between ASC and iron species drives two competing loops (Figure 1c). The catalytic pathway (blue loop) regenerates  $H_2O_2$ , potentially leading to ROS accumulation. In contrast, the redox pathway (orange loop) reduces  $Fe^{3+}$  to  $Fe^{2+}$ , driving the Fenton reaction to generate  $[Fe(IV)=O]^{2+}$  and hydroxyl radicals. These intermediates subsequently oxidize methyl-containing organosulfur compounds to produce methane while regenerating  $Fe^{3+}$  for the next cycle. Consequently, determining the dominant microkinetic pathway is essential to distinguish between the ROS regeneration and the methane production loop. Based on this, we hypothesize that methane production proceeds via ferryl ions and methyl group-containing organosulfur compounds such as methionine (MET), through the pathway described in Eq. 9 (Table 2).



The ROS regeneration loop may produce  $\text{H}_2\text{O}_2$  continuously and cause cell damage, however, the generation of  $\bullet\text{OH}$  and  $[\text{Fe}^{\text{IV}}=\text{O}]^{2+}$  as intermediates in the Fenton-driven methane production loop may contribute to methane production. Addressing the counteracting effects of the ROS regeneration loop and the Fenton-driven methane production loop would require the preferred reaction for ROS-driven methane production microkinetics to be established. To this end, microkinetic simulation was used to determine which reaction cycle (the orange, or blue), or both reaction cycles shown in Figure 1c is more favorable.

Microkinetic simulation can be conducted using both quantum and classical computing algorithms, each offering its own set of advantages. Most recently, the Harrow Hassidim and Lloyd (HHL) quantum algorithm has been successfully applied in solving linear microkinetic matrices.<sup>18, 19</sup> The Levenberg-Marquardt (LM) classical algorithm has already been used to determine the microkinetic parameters with nonlinear matrices.<sup>20-22</sup> These studies have demonstrated the versatility of microkinetic simulation and its potential to couple both quantum and classical computing approaches.

In the context of ROS-driven methane production microkinetics, the mass balance of the reaction between ASC and  $\text{Fe}^{3+}$  can be formulated as a system of linear equations, whereas that of the associated reactions between ferryl ion and MET can be modelled non-linearly. This study, thus, aims to achieve three objectives: 1) determine the microkinetic model between ASC and  $\text{Fe}^{3+}$  using the quantum HHL algorithm, 2) employ the classical LM algorithm to calculate the microkinetics between ferryl ion and MET, and 3) simulate the ROS-driven methane-forming microkinetics using the HHL algorithm. The quantum HHL simulation results were benchmarked against classical



computations, with further validation conducted against existing experimental data from relevant studies. Additionally, the microkinetics of ROS scavenging, ASC, oxygen, and iron species for ROS-driven methane production will be discussed. The findings of this study will advance our understanding of ROS-driven methane production in natural and engineered systems. Moreover, the insights for future research studies associated with applying quantum and classical computing simulations in microkinetic models are addressed.

## 2. Methodology

### 2.1 Simulation parameters and assumptions

To develop our microkinetic simulation, we utilized experimental data from Althoff et al., who investigated abiotic methane formation from organosulfur compounds (MET) in the presence of iron, ascorbate, and H<sub>2</sub>O<sub>2</sub>.<sup>11, 23</sup> We adopted their reported reactant concentrations and environmental conditions to define the initial settings for our computational model (Table 1).

**Table 1.** Reactants and reaction conditions used in the analysis.<sup>11, 23</sup>

Reactant	Concentration (mmol/L)
ASC	50
Ferric ion	40
MET	0.5
Hydrogen peroxide	100
Dissolved oxygen	160
Condition	Value
pH value	3
Temperature	25°C
Reaction time	30 h
Reaction volume	1 mL

In this simulation, a pH of 3 was selected for the following reasons: 1) Previous research indicated a maximum ROS-driven methane production at pH = 3 based on experiments conducted in the pH



range of 1-9.<sup>11</sup> 2) In our case, ROS-driven methane production in *E. coli* likely occurs in the *E. coli* periplasmic cell envelope, where its pH is in the range of pH = 1-3.<sup>24</sup> Since such a pathway is applicable to all organisms, it is plausible to have it in the *E. coli* periplasm.<sup>3</sup> Moreover, ASC formation by *E. coli* has been reported previously, indicating its capability to survive in acidic conditions.<sup>25</sup> Furthermore, *E. coli*, possesses regulatory hydrogenase that can effectively ensure its survival under lower pH conditions (pH  $\geq$  2).<sup>26</sup> 3) Some archaeal species can still be active even at pH = 1-2.<sup>27</sup> 4) The cytoplasmic proteins of acetogens remain stable under extremely acidic conditions.<sup>28</sup> Therefore, ROS-driven methane production pathways may occur in organisms at low pH.

Table 2 provides a summary of the stoichiometry, reaction kinetics, and thermodynamic constants used for the microkinetic simulations. Here, Eqs. 1- 7 were used to describe the interactions between different reactants. The chemical reactions Eqs. 1- 4 represent the catalytic and redox reactions between ASC and Fe<sup>3+</sup>, as well as the interactions between the corresponding products. Eqs. 5 and 6 reflect the products of the two Fenton reactions, namely •OH and [Fe<sup>(IV)</sup>=O]<sup>2+</sup>. Finally, Eq. 7 reflects the role of ASC in scavenging •OH.

To establish the microkinetic model, several assumptions were made: 1) The molar concentration of DHA in Eq. 1 and Eq. 4 shown in Table 2 was taken to be the same as the concentration of HO<sub>2</sub><sup>-</sup> and H<sub>2</sub>O<sub>2</sub>, according to the stoichiometric ratio of 1:1; 2) The concentration of DHA has a linear relationship with Fe<sup>3+</sup>;<sup>29</sup> 3) The concentration of O<sub>2</sub><sup>-</sup> is 3.9 mM, using a conversion rate of 1.5% for [O<sub>2</sub>] to [O<sub>2</sub><sup>-</sup>] according to previous literature;<sup>30</sup> 4) Eq. 2 and Eq. 3 can be combined as Eq. 8 in Table 2, and since Eq.3 is the rate limiting reaction, the kinetic reaction rate constant can be taken



as  $k_3$ , 5) The interaction pathway between  $[\text{Fe}^{\text{IV}}=\text{O}]^{2+}$  and MET, as proposed by Althoff et al., can be summarized as Eq. 9 in Table 2. <sup>11</sup> 6) Reactions Eq. 5 and Eq. 7 can be combined as Eq.10 in Table 2, and the kinetic reaction rate constant can be taken as  $k_5$  (rate limiting).

View Article Online

DOI: 10.1039/D5VA00420A





**Table 2.** Reactions used in this analysis and their standard Gibbs free energies and reaction rate constants at 25 °C

	Reaction	Kinetic parameter ( <i>k</i> ) (M <sup>-1</sup> s <sup>-1</sup> )	Referenc e	Gibbs free energy ( $\Delta G_{\theta}$ ) (kcal/mol)	Referenc e
(1)	ASC + Fe <sup>3+</sup> + O <sub>2</sub> = DHA + Fe <sup>3+</sup> +H <sub>2</sub> O <sub>2</sub>	$k_1 = 4.0 \times 10^5$	31	$\Delta G_{0-1} = -10.2$	32, 33*a
(2)	ASC + Fe <sup>3+</sup> = Fe <sup>2+</sup> + 2H <sup>+</sup> + A <sup>·-</sup>	$k_2 = 4.5 \times 10^3$	34	$\Delta G_{0-2} = 1.1$	35
(3)	Fe <sup>2+</sup> + O <sub>2</sub> = Fe <sup>3+</sup> + O <sub>2</sub> <sup>·-</sup>	$k_3 = 1.0 \times 10^{-5}$	36	$\Delta G_{0-3} = -91.6$	37
(4)	A <sup>·-</sup> + O <sub>2</sub> <sup>·-</sup> + H <sub>2</sub> O = DHA + HO <sub>2</sub> <sup>-</sup> + OH <sup>-</sup>	$k_4 = 2.6 \times 10^8$	38	$\Delta G_{0-4} = 38.4$	39
(5)	Fe <sup>2+</sup> + H <sub>2</sub> O <sub>2</sub> = Fe <sup>3+</sup> + ·OH + OH <sup>-</sup>	$k_5 = 5.7 \times 10^2$	40	$\Delta G_5 = 28.7$	*b
(6)	Fe <sup>2+</sup> + H <sub>2</sub> O <sub>2</sub> = [Fe <sup>IV</sup> =O] <sup>2+</sup> + H <sub>2</sub> O	$k_6 = 1.0 \times 10^6$	41	$\Delta G_6 = -14.9$	*c
(7)	ASC + ·OH = A <sup>·-</sup> + H <sub>2</sub> O + H <sup>+</sup>	$k_7 = 7.9 \times 10^9$	16	$\Delta G_7 = -30.4$	*b
(8)	ASC + O <sub>2</sub> = 2H <sup>+</sup> + O <sub>2</sub> <sup>·-</sup> + A <sup>·-</sup>	-	*d	-	*d
(9)	2[Fe <sup>IV</sup> =O] <sup>2+</sup> + MET+ H <sub>2</sub> O <sub>2</sub> + 2H <sup>+</sup> = 2Fe <sup>3+</sup> + HCyA + CH <sub>4</sub> + H <sub>2</sub> O	-	*d	-	*d
(10)	ASC + Fe <sup>2+</sup> + H <sub>2</sub> O <sub>2</sub> = Fe <sup>3+</sup> +A <sup>·-</sup> + 2H <sub>2</sub> O	-	*d	-	*d

\*a: The  $\Delta G_{0-1}$  was calculated using the relationship  $\Delta G_{\theta} = -nFE_{\text{cell}}$ , where  $n=2$  and  $F$  is the Faraday constant.  $E_{\text{cell}}$  is the change of total reaction reduction potential, which was obtained between  $E_{(\text{O}_2/\text{H}_2\text{O}_2)} = +0.28\text{V}$  and  $E_{(\text{dehydroascorbate/ascorbate})} = +0.06\text{V}$ .<sup>32, 33</sup>

\*b: The  $\Delta G$  value was calculated based on the standard Gibbs free energies of formation  $\Delta G_f$  for the individual chemical species.<sup>35, 42, 43</sup>

\*c: Calculated using the equilibrium constant (K) estimated from the MATLAB kinetic simulation.

\*d: Refer to section 2.1 and Supplementary Table 1.

**Note:** Enzymatic scavengers (SOD, Catalase) are excluded in this study. Their presence in vivo regulates ROS levels but does not alter the fundamental role of Ferryl iron in driving methane formation.



## 2.2 Kinetic estimation using HHL algorithm

In this study, the HHL algorithm was used to simulate microkinetic models to determine the mechanism behind ASC, Fe<sup>3+</sup>, and the ROS-driven methane production (redox and/or catalysis pathway). We constructed the model according to the chemical equilibrium principle that the rates of forward reaction and reverse reaction are equivalent. The forward reaction rate constant ( $k$ ) and Gibbs free energy ( $\Delta G_0$ ) used are shown in Table 2 and in the Supplementary Table 1. Detailed calculations are shown in the Supplementary Note 1.

To investigate the mechanism for ROS-driven methane production microkinetics in non-methanogenic microbes at the conditions listed in Table 1, the following system of linear equations was built.

$$A \cdot x = b \quad (11)$$

where  $A$  and  $b$  are known matrices while  $x$  is the unknown matrix to be determined.

The HHL algorithm requires matrix  $A$  to be Hermitian, necessitating the transformation of  $A$  into matrix  $A^H$ .

$$A^H = \begin{bmatrix} 0 & A \\ A^\dagger & 0 \end{bmatrix} \quad (12)$$

where  $A^\dagger$  denotes the complex conjugate transpose of  $A$ .

After the conversion of matrix ( $A$ ) of Eq. 11 into the Hermitian matrix ( $A^H$ ) in Eq. 12, the unknown



term  $x$  was calculated using Eq. 13 in the HHL algorithm:

View Article Online  
DOI: 10.1039/D5VA00420A

$$x = b \times A^{H-1} \quad (13)$$

Hence, to investigate whether the redox and/or catalysis pathway drives the reaction between ASC and  $\text{Fe}^{3+}$ , a microkinetic linear matrix model (Eq. 14) was constructed based on Eqs. 1, 4 and 8 at steady state. The procedure for establishing Eq. 14 is shown in the Supplementary Note 2.

$$\begin{bmatrix} \frac{1}{50 \times 10^{-3}} & \frac{1}{50 \times 10^{-3}} & \frac{1}{50 \times 10^{-3}} & \frac{1}{50 \times 10^{-3}} \\ k_1 & 0 & -k_{-1}[\text{DHA}] & 0 \\ 0 & -k_4[\text{OH}^-][\text{DHA}] & 0 & k_4[\text{O}_2 \cdot^-] \\ k_3 & 0 & 0 & -k_{-3}[\text{H}^+]^2[\text{O}_2 \cdot^-] \end{bmatrix} \times \begin{bmatrix} \text{ASC} \\ \text{HO}_2^- \\ \text{H}_2\text{O}_2 \\ \text{A} \cdot^- \end{bmatrix} = \begin{bmatrix} 1 \\ 0 \\ 0 \\ 0 \end{bmatrix} \quad (14)$$

To investigate the ROS-driven methane production pathway, a microkinetic linear matrix (Eq. 15) was built initially to simulate the probability of the Fenton reaction forming  $[\text{Fe}^{\text{IV}}=\text{O}]^{2+}$  to participate in the ROS-driven methane production pathway. Eq. 15 was constructed based on reactions Eqs. 2, 6 and 10 at steady state. The process for establishing Eq. 15 is given in the Supplementary Note 3.

$$\begin{bmatrix} \frac{1}{40 \times 10^{-3}} & \frac{1}{40 \times 10^{-3}} & \frac{1}{40 \times 10^{-3}} & 0 \\ k_2[\text{ASC}] & -k_{-2}[\text{H}^+]^2[\text{A} \cdot^-] & 0 & 1 \\ -k_{-5}[\text{A} \cdot^-] & k_5[\text{ASC}][\text{H}_2\text{O}_2] & 0 & 1 \\ 0 & k_6[\text{H}_2\text{O}_2] & -k_{-6} & 0 \end{bmatrix} \times \begin{bmatrix} \text{Fe}^{3+} \\ \text{Fe}^{2+} \\ \text{Fe}^{\text{IV}}=\text{O}^{2+} \\ \text{c} \end{bmatrix} = \begin{bmatrix} 1 \\ 0 \\ 0 \\ 0 \end{bmatrix} \quad (15)$$

To investigate the methane production of MET oxidated  $[\text{Fe}^{\text{IV}}=\text{O}]^{2+}$  in the ROS-driven methane production pathway, a microkinetic linear matrix model (Eq. 16) was constructed based on the Eq. 9 reaction at steady state. According to the stoichiometric ratio in the Eq. 9 reaction, the production of HCYA represents methane production. The process for establishing Eq. 16 is shown in the Supplementary Note 3.



$$\begin{bmatrix} \frac{1}{k_9[\text{Fe}^{\text{IV}}=\text{O}^{2+}]^2[\text{H}_2\text{O}_2][\text{H}^+]^2} & \frac{1}{-k_9[\text{Fe}^{3+}]^2} \end{bmatrix} \times \begin{bmatrix} \text{MET} \\ \text{HCyA} \end{bmatrix} = \begin{bmatrix} 1 \\ 0 \end{bmatrix} \quad (16)$$

### 2.3 Kinetic estimation using LM algorithm

The reaction rate constant between MET and  $[\text{Fe}^{\text{(IV)}=\text{O}}]^{2+}$  was determined using mass balances derived from reaction Eqs. 2, 5, 6, 7 and 9. The resulting non-linear matrix (Eq. 17) was solved using MATLAB with a LM algorithm. Further information about the matrix development is given in Supplementary Note 4.

$$\begin{bmatrix} N_{\text{Fe}^{2+}, \text{Final}} \\ N_{\text{H}_2\text{O}_2, \text{Final}} \\ N_{\text{Fe}^{3+}, \text{Final}} \\ N_{\text{OH}, \text{Final}} \\ N_{\text{CH}_4, \text{Final}} \\ N_{\text{ASC}, \text{Final}} \\ N_{\text{Fe}^{\text{IV}}\text{O}^{2+}, \text{Final}} \\ N_{\text{MET}, \text{Final}} \end{bmatrix} - \begin{bmatrix} -k_5-k_6 & k_2 & 0 & 0 \\ -k_5-k_6 & 0 & 0 & 0 \\ k_5 & k_2 & 0 & 0 \\ k_5 & 0 & -k_7 & 0 \\ 0 & 0 & 0 & k_9 \\ 0 & 0 & 0 & 0 \\ 0 & -k_2 & -k_7 & 0 \\ 0 & 0 & 0 & -k_9 \\ 0 & 0 & 0 & -k_9 \end{bmatrix} \cdot \begin{bmatrix} [\text{Fe}^{2+}] \cdot [\text{H}_2\text{O}_2] \\ [\text{Fe}^{3+}] \cdot [\text{ASC}] \\ [\text{Fe}^{3+}] \cdot [\text{OH}] \\ [\text{Fe}^{\text{IV}}=\text{O}^{2+}]^2 [\text{MET}] [\text{H}_2\text{O}_2] [\text{H}^+]^2 \end{bmatrix} \cdot V \cdot t - \begin{bmatrix} N_{\text{Fe}^{2+}, \text{Initial}} \\ N_{\text{H}_2\text{O}_2, \text{Initial}} \\ N_{\text{Fe}^{3+}, \text{Initial}} \\ N_{\text{OH}, \text{Initial}} \\ N_{\text{CH}_4, \text{Initial}} \\ N_{\text{ASC}, \text{Initial}} \\ N_{\text{Fe}^{\text{IV}}\text{O}^{2+}, \text{Initial}} \\ N_{\text{MET}, \text{Initial}} \end{bmatrix} = 0 \quad (17)$$

where V denotes the reaction volume, and t refers to the reaction time.



## 3. Results

View Article Online  
DOI: 10.1039/D5VA00420A

### 3.1 Mechanistic determination analysis

Table 3 summarizes the simulated concentrations of the reaction products,  $[\text{HO}_2^-]$ ,  $[\text{A}^\cdot]$  and  $[\text{H}_2\text{O}_2]$  associated with ASC and  $\text{Fe}^{3+}$  participation in redox and catalytic reactions, respectively. The results obtained using the quantum HHL algorithm showed good agreement with the classical MATLAB simulation. Notably, regarding the catalytic product  $[\text{HO}_2^-]$ , the classical simulation yielded a value of  $\sim 10^{-20}$  mol/L. It is important to clarify that this non-zero value represents a numerical artifact (asymptotic residue) inherent to classical ODE solvers using floating-point arithmetic, rather than a physical concentration. In contrast, the quantum simulation reported a concentration of 0.00 mol/L, correctly identifying the absence of this species within the algorithmic resolution.

Consequently, both simulations confirmed that nearly 100% of the reaction proceeded via the redox pathway. This result was consistent with the fact that the Gibbs free energy for Eq. 8 ( $\Delta G = -90.5$  kcal/mol) is significantly more negative than that for Eq. 1 ( $\Delta G = -10.2$  kcal/mol), indicating a strong thermodynamic preference for the redox pathway. In the presence of oxygen, ASC, and  $\text{Fe}^{3+}$ ,  $\text{A}^\cdot$  generation by Eq. 8 is more favorable. Eq. 8 is dependent on the redox reaction between ASC and  $\text{Fe}^{3+}$  occurring, rather than the catalytic reaction. These findings aligned well with the results of the studies conducted by Timoshnikov et al. and Buettner & Jurkiewicz, which showed the high degree of  $\text{Fe}^{3+}$  reduction by ASC under aerobic conditions and at a pH of 3.<sup>15, 44</sup> The simulation results showed that ASC is beneficial for promoting methane production in the Fenton-driven methane production loop. Thus, the redox reaction between ASC and  $\text{Fe}^{3+}$  plays a decisive role in tilting the microkinetics towards the ROS-driven methane production pathway.



**Table 3.** Summary of the simulation results

Unknown parameter	Estimated values (Quantum)	Estimated values (Classical)	Remarks	Error
<i>Mechanistic determination by Google Quantum AI &amp; Classical MATLAB</i>				
[ASC]	0.00 (mol/L)	0.00 (mol/L)	-	
[HO <sub>2</sub> <sup>-</sup> ]	0.00 (mol/L)	1.56 × 10 <sup>-20</sup> (mol/L)	Redox reaction <sup>*a</sup>	1.56 × 10 <sup>-20</sup>
[H <sub>2</sub> O <sub>2</sub> ]	0.00 (mol/L)	0.00 (mol/L)	Catalytic reaction <sup>*a</sup>	
[A <sup>-</sup> ]	5.00 × 10 <sup>-2</sup> (mol/L)	5.00 × 10 <sup>-2</sup> (mol/L)	Redox reaction <sup>*a</sup>	
<i>Kinetic reaction rate constant determination by Classical MATLAB</i>				
$k_9$ <sup>*b</sup>	-	1.83 × 10 <sup>-4</sup> (M <sup>-1</sup> s <sup>-1</sup> )	-	-
<i>Microkinetic simulation by Google Quantum AI &amp; Classical MATLAB</i>				
[Fe <sup>3+</sup> ]	0.00 (mol/L)	2.93 × 10 <sup>-7</sup> (mol/L)	0 <sup>*c</sup>	4.14 × 10 <sup>-7</sup>
[Fe <sup>2+</sup> ]	0.00 (mol/L)	1.20 × 10 <sup>-11</sup> (mol/L)	0 <sup>*c</sup>	
[Fe <sup>IV</sup> =O <sup>2+</sup> ]	4.00 × 10 <sup>-2</sup> (mol/L)	4.00 × 10 <sup>-2</sup> (mol/L)	100% <sup>*c</sup>	
[MET]	4.71 × 10 <sup>-4</sup> (mol/L)	4.71 × 10 <sup>-4</sup> (mol/L)	-	1.23 × 10 <sup>-12</sup>
N <sub>Methane</sub> <sup>*d</sup>	4.71 × 10 <sup>-8</sup> mol	4.71 × 10 <sup>-8</sup> mol	-	
Conversion rate <sup>*e</sup>		9.42%	This work	-
Conversion rate <sup>*f</sup>		10.00%	Althoff et al. <sup>11</sup>	-

Note: Classical results include a numerical artifact from ODE solvers. The residual values ( $\sim 10^{-7}$ ) for trace species are negligible in representing physical concentrations.

\*a: Products of catalytic/redox reaction indicated in Eq. 14.

\*b:  $k_9$  is the kinetic parameter for Eq. 9.

\*c: The proportion of iron ions involved in Fenton reaction.

\*d: Methane production.

\*e: Simulated conversion rate ( $\eta$ ) of MET to methane in Google Quantum AI.

\*f: Experimentally measured conversion rate ( $\eta$ ) of MET to methane conducted by Althoff et al.<sup>11</sup>

### 3.2 Kinetic reaction rate constant determination

The kinetic rate constant  $k_9$  in the matrix (Eq. 17) was derived as  $1.83 \times 10^{-4} \text{ M}^{-1}\text{s}^{-1}$  (Table 3) by implementing the LM algorithm in MATLAB. Comparing the reactions represented by Eq. 6 and Eq. 9, the reaction rate constant ( $k_9$ ) between [Fe<sup>(IV)</sup>=O]<sup>2+</sup> and MET is approximately ten orders of



magnitude lower than the reaction rate constant ( $k_6$ ) of the Fenton reaction to produce  $[\text{Fe}^{\text{(IV)}}=\text{O}]^{2+}$ ,  
implying that the reaction of  $[\text{Fe}^{\text{(IV)}}=\text{O}]^{2+}$  and MET is the rate-determining step in the ROS-driven  
methane production pathway. Supplementary Table 2 provides a summary of the MATLAB output  
results.

### 3.3 Microkinetic simulation

The results derived from the execution of Eq. 15 matrix on Google Quantum AI platform were  
consistent with classical MATLAB computations (Table 3). It is evident that through the Fenton  
reaction, iron is prone towards ferryl ion formation ( $4.00 \times 10^{-2}$  (mol/L), with near 100% conversion  
rate from iron to ferryl ion. This result matched the findings of Deguillaume et al., which showed  
that at a low pH of 3.5, the concentration of ferryl ion produced by the reaction of  $\text{Fe}^{2+}$  and  $\text{H}_2\text{O}_2$   
was  $10^4$  times greater than the concentration of  $\bullet\text{OH}$  produced.<sup>45</sup> From the microkinetics  
perspective, the kinetic reaction rate constant between  $\text{Fe}^{3+}$  and  $\text{H}_2\text{O}_2$  to produce ferryl ion ( $k_6$ ) is  
 $10^4$  times greater than that of  $\bullet\text{OH}$  formation ( $k_5$ ) in the ROS-driven methane production process.  
 $\text{Fe}^{3+}$  ( $k_2$ ) and  $\bullet\text{OH}$  ( $k_7$ ) exhibit a greater susceptibility to reduction by ASC as compared to  $k_5$ . As a  
result, the ferryl ion serves as a primary reactant with MET to produce methane.

According to the stoichiometric ratio in Eq. 9, the product concentration of HCyA is directly  
proportional to the methane produced. Therefore, methane production can be estimated using Eq.  
16 through the HHL algorithm. In addition, the conversion rate ( $\eta$ ) of MET to methane can be  
calculated. The quantum-simulated conversion rate ( $\eta$ ) was 9.42% (Table 3), showing strong  
agreement with the classical calculation (10.00%) and the experimental value reported by Althoff  
et al.<sup>11</sup> The detailed calculations are shown in Supplementary Note 5.



## 4. Discussion

### *4.1 Effect of radical kinetics and oxygen levels for methane production*

An investigation of the •OH concentration in cells is of paramount importance. In the ROS-driven methane production pathway studied in this work (conditions presented in Table 1), •OH produced by the Fenton reaction (Figure 1c), can either react with methyl compounds to form methane or be scavenged by ASC. ASC reportedly has a strong affinity for •OH with a high reaction rate of  $7 \times 10^9 \text{ M}^{-1}\text{s}^{-1}$ .<sup>46</sup> Meanwhile, the reaction rate constant of •OH attacking intracellular DNA is  $3 \times 10^8 \text{ M}^{-1}\text{s}^{-1}$ .<sup>47</sup> This difference in the order of magnitude indicates that the scavenging effect of ASC occurs at a higher rate than •OH-induced cellular damage. As a result, it is proposed that ROS in the methane production pathway does not cause significant damage to cells. Furthermore, the reaction rate constant of methyl-containing compounds and •OH is  $1.5 \times 10^7 \text{ M}^{-1}\text{s}^{-1}$ , which is notably lower than the scavenging rate of •OH by ASC ( $7 \times 10^9 \text{ M}^{-1}\text{s}^{-1}$ ).<sup>48</sup> Therefore, the contribution of •OH may not be as significant as that of ferryl ions in the ROS-driven methane production pathway.



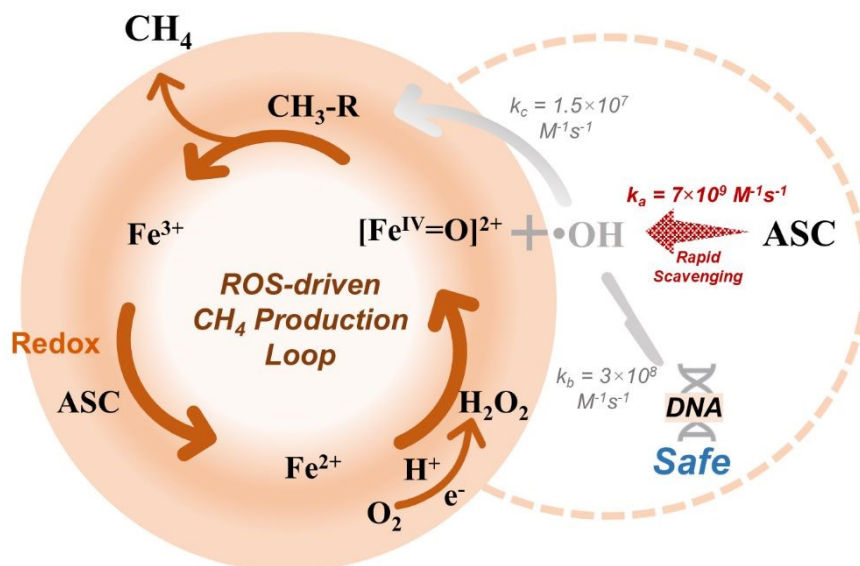


**Figure 2.** Schematic indicating that  $\bullet\text{OH}$  (the product of the Fenton reaction) does not participate in the ROS-driven  $\text{CH}_4$  production loop and damages intracellular DNA.  $k_a$  is the reaction rate constant between ASC and  $\bullet\text{OH}$ ;  $k_b$  is the reaction rate constant between DNA and  $\bullet\text{OH}$ ;  $k_c$  is the reaction rate constant between methyl-containing compounds and  $\bullet\text{OH}$ .<sup>48</sup>

Our findings mechanistically demonstrate the feasibility of a ROS-driven methane production pathway under the specific abiotic conditions modeled. This pathway offers a theoretical framework to interpret methane enhancement phenomena not only in micro-aeration anaerobic digestion (MAAD), but also in natural systems, such as wetlands.<sup>6, 49</sup> While these systems can synthesize  $\text{H}_2\text{O}_2$  under oxygen ( $\sim 21$   $\mu\text{M}$  in wetlands vs. 270-290  $\mu\text{M}$  in MAAD), which reacts with  $\text{Fe}^{2+}$  to promote the generation of ferryl ions and facilitates the conversion of MET to methane.<sup>8, 50, 51</sup> Extrapolating these microkinetic results to complex environmental matrices introduces inherent uncertainties. Factors such as pH variations, organic ligand complexation, and microbial interactions in natural ecosystems may significantly alter the reaction kinetics compared to our simplified model. Recent studies suggest that ROS can promote Fenton reaction in bacteria and archaea, generating ferryl ions that oxidize methyl-containing donors.<sup>3</sup> These biological observations align with our mechanistic findings; however, distinguishing the specific contribution of this ROS-driven pathway



from canonical enzymatic processes in diverse oxygen environments requires further *in situ* validation to bridge the gap between idealized modeling and ecosystem complexity.

However, excessively high oxygen levels may negatively impact the overall methane production in these systems. For instance, in cyanobacteria, the conversion rate of organic MET is affected when the oxygen concentration is close to that of air-saturated water.<sup>23, 50</sup> Higher intracellular oxygen levels have been shown to lower the conversion rates for both MET (about 10%) and  $[\text{Fe}^{\text{IV}}=\text{O}]^{2+}$ .<sup>11</sup> In addition, Althoff et al. reported a lack of  $\text{CH}_4$  formation in an oxygen-saturated environment, most likely due to oxygen's adverse effects on ROS-driven methane production.<sup>23</sup> This might be attributed to the reaction between the methyl radical ( $\cdot\text{CH}_3$ ), the methane precursor, and  $\text{O}_2$ , forming methylperoxyl ( $\text{CH}_3\text{OO}\cdot$ ) with a significantly high reaction rate constant of  $3.7 \times 10^9 \text{ M}^{-1}\text{s}^{-1}$ .<sup>51</sup> The formation of methylperoxyl reduces the production of methane. This rate constant for the reaction between  $\cdot\text{CH}_3$  and  $\text{O}_2$  is notably larger than the calculated rate constant for the methane production reaction of  $[\text{Fe}^{\text{IV}}=\text{O}]^{2+}$  with MET ( $1.83 \times 10^{-4} \text{ M}^{-1}\text{s}^{-1}$ ) investigated in this study. Aside from ROS-driven methane production, oxygen overload also affects methanogenesis by creating an unfavorable environment for methanogens' survival, lowering the overall methane production rate.<sup>2</sup> Hence, ascertaining the oxygen concentration threshold required for striking a balance between ROS-induced and methanogen-based methane production would be advantageous for engineered systems such as MAAD seeking enhanced methane production as well as the control and mitigation of methane emission from natural ecosystems. Future work must bridge the gap between this idealized microkinetic model and *in situ* environmental conditions to validate these broader implications.



## 4.2 Perspectives and limitations of microkinetic using quantum computing

View Article Online  
DOI: 10.1039/D5VA00420A

Quantum computing incorporates the superposition and entanglement properties of quantum mechanics and can surpasses classical computation in analyzing and quantifying information under certain conditions. Notably, it can efficiently simulate the energy consumption of the Haber-Bosch process (1 - 2% of global energy consumption), an energy-intensive process, by analyzing the underlying chemical reaction mechanisms.<sup>52</sup> Specifically, the HHL algorithm enables the implementation of chemical microkinetic models on quantum computers, for processes such as CO oxidation, aiding in the resolution of chemical kinetics-related issues.<sup>19, 53</sup> Furthermore, Becerra et al. used the same quantum algorithm to quantify the uncertainties in Rh(III)-catalyzed CO oxidation pathways, which classical computation struggles to calculate. This emerging trend suggests that quantum computing may be a promising technique for simulating chemical reaction mechanisms and microkinetic models.<sup>18, 54</sup> It foreshadows the potential mainstream adoption of quantum simulation for predicting molecular properties, activation energies, and reaction rate constants.<sup>55, 56</sup>

While classical solvers remain efficient for these small-scale systems, this study establishes a prospective algorithmic advantage. By replacing classical polynomial scaling (e.g.,  $O(N^3)$  for matrix inversion), the HHL algorithm offers an exponential speedup with logarithmic scaling ( $O(\log N)$ )<sup>57</sup>. To illustrate this, for a hypothetical large-scale network with  $N=10^6$  species, classical computational cost would surge to  $10^{18}$  operations, whereas the quantum complexity grows only to the order of  $\log(10^6)$  (approx. 20). Nevertheless, this scaling analysis indicates that quantum solvers will be indispensable for future large-scale biochemical reaction network simulations, where high



dimensionality renders classical approaches computationally prohibitive. This capability will enable the study of more complex environments for further investigation and related systems in the future.

Variations in the oxygen content of organisms may have an impact on ROS concentration, thereby influencing variations in the methane content.<sup>9</sup> Consequently, this study investigated the impact of oxygen concentration in the range of 0 -1000 mM in the models. The concentration of  $O_2^{\cdot-}$  in the initial model is influenced by the oxygen content, consequently affecting the relative importance of the redox and catalysis reactions. However, the results have shown that the redox reaction dominated within this oxygen concentration range, as detailed in Supplementary Figure 1. For the microkinetic simulation of ROS-induced methane production modelling, alterations in oxygen concentration ought to influence  $H_2O_2$ . However, the model's foundation is based on the chemical experimental data presented by Althoff et al.<sup>11,23</sup> Hence, the  $H_2O_2$  concentration remained constant throughout this study. Furthermore, the proportional relationship between the conversion of oxygen to  $H_2O_2$  within living organisms remains unclear and it is not known how much oxygen can be converted into  $H_2O_2$  within a cell. A comprehensive investigation into the influence of oxygen concentration on methane production in methanogenic pathways driven by ROS is thus unattainable. Moreover, the simulation of this work was largely based on the experimental data of Althoff et al., obtained through the reactions of pure chemicals at pH 3.<sup>11</sup> There is a lack of research on ROS-driven methane production in organisms at higher biological pH. In nature and environmental systems such as anaerobic digesters, which operate at circumneutral pH (6.5–8.0), iron speciation differs significantly, often involving precipitation or complexation with organic ligands.<sup>58</sup> These structural changes alter reaction energy barriers and kinetic rate constants ( $k$ ). To extend our algorithmic framework to these conditions, we propose a hybrid computational strategy: theoretical



methods like Density Functional Theory (DFT) or the Variational Quantum Eigensolver (VQE) can be employed to calculate the specific activation energies and rate constants for iron-ligand complexes at neutral pH.<sup>59,60</sup> Additionally, experimental techniques such as Electron Paramagnetic Resonance (EPR) spectroscopy could be integrated in future studies to directly detect the transient ferryl iron intermediates predicted by our model.<sup>61</sup> These derived parameters can then serve as updated inputs for the HHL solver, ensuring the model's applicability across diverse biochemical settings.

From a biological perspective, fermentative bacteria, which are known for their ability to survive and function well in a wide pH range (4–8), could serve as better candidates to study this phenomenon.<sup>62</sup> The intracellular pH is generally lower than the extracellular pH, reaching 3.5 to 4.5.<sup>63</sup> Methods to study methane production *in vivo* such as microbial electro-methanogenesis, may be used to explore ROS-driven methane production at pH 3.5 to 7.5 in future investigations.<sup>64</sup>

## 5. Conclusion

This study employed a hybrid quantum-classical computational framework to investigate the microkinetics of ROS-driven methane production. The results indicate that the redox reaction between ASC and  $\text{Fe}^{3+}$  is favored over the catalytic pathway, thereby supporting continued Fenton-driven methane production through  $\text{Fe}^{2+}$  regeneration. The reaction between  $[\text{Fe}(\text{IV})=\text{O}]^{2+}$  and MET was identified as the rate-determining step, and the quantum simulated MET to methane conversion rate showed good agreement with current experimental observations, supporting the proposed mechanistic pathway.

View Article Online  
DOI: 10.1039/D5VA00420A



These findings identify a feasible abiotic pathway for ROS-driven methane production and provide a theoretical framework for interpreting methane enhancement phenomena in micro-aeration anaerobic digestion and potentially in natural systems such as wetlands. More broadly, this work demonstrates the potential of the HHL quantum algorithm for microkinetic modelling, particularly in larger biochemical reaction networks where classical computation may become challenging. Further experimental validation under more complex biological conditions will be important for extending the applicability of this framework.

#### **CRedit authorship contribution statement**

**Ronghan Zhang and Zexuan Wang:** Conceptualization, Methodology, Software, Formal analysis, Investigation, Writing – original draft, Writing – review & editing. **Kin Tung Michael Ho:** Conceptualization, Writing – review & editing. **Nigel J.D. Graham:** Writing – review & editing. **Giin-Yu Amy Tan:** Writing – review & editing. **Po-Heng Lee:** Supervision, Conceptualization, Writing – review & editing.

#### **Acknowledgements**

The authors gratefully acknowledge Prof. Aleksandra Szczuka from the Department of Civil and Environmental Engineering, University of Michigan, Ann Harbour, for her valuable input in modelling and reviewing the paper.

#### **Conflict of interest**

The authors declare no competing financial interest.



## SUPPORTING INFORMATION

View Article Online  
DOI: 10.1039/D5VA00420A

Supporting information is available at ... .

**Code Availability:** The source code underlying the results presented in this study is available in the Supplementary Materials.

## References

1. S. Biswas, A. P. Kulkarni, S. Giddey and S. Bhattacharya, A review on synthesis of methane as a pathway for renewable energy storage with a focus on solid oxide electrolytic cell-based processes, *Frontiers in Energy Research*, 2020, **8**, 570112.
2. N. Yu, B. Guo, Y. Zhang, L. Zhang, Y. Zhou and Y. Liu, Different micro-aeration rates facilitate production of different end-products from source-diverted blackwater, *Water Research*, 2020, **177**, 115783.
3. L. Ernst, B. Steinfeld, U. Barayeu, T. Klintzsch, M. Kurth, D. Grimm, T. P. Dick, J. G. Rebelein, I. B. Bischofs and F. Keppler, Methane formation driven by reactive oxygen species across all living organisms, *Nature*, 2022, **603**, 482-487.
4. S. Montalvo, F. Ojeda, C. Huiliñir, L. Guerrero, R. Borja and A. Castillo, Performance evaluation of micro-aerobic hydrolysis of mixed sludge: Optimum aeration and effect on its biochemical methane potential, *Journal of Environmental Science and Health, Part A*, 2016, **51**, 1269-1277.
5. S.-F. Fu, F. Wang, X.-S. Shi and R.-B. Guo, Impacts of microaeration on the anaerobic digestion of corn straw and the microbial community structure, *Chemical Engineering Journal*, 2016, **287**, 523-528.
6. D. Nguyen and S. K. Khanal, A little breath of fresh air into an anaerobic system: How microaeration facilitates anaerobic digestion process, *Biotechnology advances*, 2018, **36**, 1971-1983.
7. Q. Chen, W. Wu, D. Qi, Y. Ding and Z. Zhao, Review on microaeration-based anaerobic digestion: State of the art, challenges, and perspectives, *Science of the Total Environment*, 2020, **710**, 136388.
8. X. Liu, D. Huang, C. Zhu, F. Zhu, X. Zhu and D. Zhou, Production of reactive oxygen species



during redox manipulation and its potential impacts on activated sludge wastewater treatment processes, *Environmental Science & Technology*, 2024, **58**, 23042-23052. View Article Online  
DOI: 10.1039/D5VA00420A

9. J. C. Angle, T. H. Morin, L. M. Solden, A. B. Narrowe, G. J. Smith, M. A. Borton, C. Rey-Sanchez, R. A. Daly, G. Mirfenderesgi and D. W. Hoyt, Methanogenesis in oxygenated soils is a substantial fraction of wetland methane emissions, *Nature communications*, 2017, **8**, 1567.
10. A. V. Borges, W. Champenois, N. Gypens, B. Delille and J. Harlay, Massive marine methane emissions from near-shore shallow coastal areas, *Scientific reports*, 2016, **6**, 27908.
11. F. Althoff, K. Benzing, P. Comba, C. McRoberts, D. R. Boyd, S. Greiner and F. Keppler, Abiotic methanogenesis from organosulphur compounds under ambient conditions, *Nature Communications*, 2014, **5**, 4205.
12. E. R. Frawley and F. C. Fang, The ins and outs of bacterial iron metabolism, *Molecular microbiology*, 2014, **93**, 609-616.
13. F. Keppler, L. Ernst, D. Polag, J. Zhang and M. Boros, ROS-driven cellular methane formation: Potential implications for health sciences. *Journal*, 2022, **12**, e905.
14. G. R. Buettner, In the absence of catalytic metals ascorbate does not autoxidize at pH 7: ascorbate as a test for catalytic metals, *Journal of biochemical and biophysical methods*, 1988, **16**, 27-40.
15. G. R. Buettner and B. A. Jurkiewicz, Catalytic metals, ascorbate and free radicals: combinations to avoid, *Radiation research*, 1996, **145**, 532-541.
16. J. Shen, P. T. Griffiths, S. J. Campbell, B. Utinger, M. Kalberer and S. E. Paulson, Ascorbate oxidation by iron, copper and reactive oxygen species: Review, model development, and derivation of key rate constants, *Scientific reports*, 2021, **11**, 7417.
17. A. Elmagirbi, H. Sulistyarti and A. Atikah, Study of ascorbic acid as iron (III) reducing agent for spectrophotometric iron speciation, *The Journal of Pure and Applied Chemistry Research*, 2012, **1**, 11-17.
18. A. Becerra, A. Prabhu, M. S. Rongali, S. C. S. Velpur, B. Debusschere and E. A. Walker, How a quantum computer could quantify uncertainty in microkinetic models, *The Journal of Physical Chemistry Letters*, 2021, **12**, 6955-6960.
19. E. A. Walker and S. A. Pallathadka, How a quantum computer could solve a microkinetic model, *The Journal of Physical Chemistry Letters*, 2020, **12**, 592-597.
20. H. P. Gavin, The Levenberg-Marquardt algorithm for nonlinear least squares curve-fitting problems, *Department of Civil and Environmental Engineering Duke University August*, 2019,



3, 1-23.

View Article Online  
DOI: 10.1039/D5VA00420A

21. K. Toch, J. Thybaut, B. Vandegheuchte, C. Narasimhan, L. Domokos and G. Marin, A Single-Event MicroKinetic model for “ethylbenzene dealkylation/xylene isomerization” on Pt/H-ZSM-5 zeolite catalyst, *Applied Catalysis A: General*, 2012, **425**, 130-144.
22. F. Jin, Y. Fan, M. Yuan, F. Min, G. Wu, Y. Ding and G. F. Froment, Single-event kinetic modeling of ethene oligomerization on ZSM-5, *Catalysis Today*, 2018, **316**, 129-141.
23. F. Althoff, A. Jugold and F. Keppler, Methane formation by oxidation of ascorbic acid using iron minerals and hydrogen peroxide, *Chemosphere*, 2010, **80**, 286-292.
24. D. He, M. Zhang, S. Liu, X. Xie and P. R. Chen, Protease-mediated protein quality control for bacterial acid resistance, *Cell Chemical Biology*, 2019, **26**, 144-150. e143.
25. Z. Zhang, M. Aboulwafa, M. H. Smith and M. H. Saier Jr, The ascorbate transporter of Escherichia coli, *Journal of bacteriology*, 2003, **185**, 2243-2250.
26. K. Noguchi, D. P. Riggins, K. C. Eldahan, R. D. Kitko and J. L. Slonczewski, Hydrogenase-3 contributes to anaerobic acid resistance of Escherichia coli, *PLoS one*, 2010, **5**, e10132.
27. C. Baker-Austin and M. Dopson, Life in acid: pH homeostasis in acidophiles, *Trends in microbiology*, 2007, **15**, 165-171.
28. J. A. Francois and T. J. Kappock, Alanine racemase from the acidophile Acetobacter aceti, *Protein expression and purification*, 2007, **51**, 39-48.
29. S. J. Campbell, B. Utinger, D. M. Lienhard, S. E. Paulson, J. Shen, P. T. Griffiths, A. C. Stell and M. Kalberer, Development of a physiologically relevant online chemical assay to quantify aerosol oxidative potential, *Analytical chemistry*, 2019, **91**, 13088-13095.
30. S. W. Schaffer and M. S. Suleiman, *Mitochondria: the dynamic organelle*, Springer Science & Business Media, 2010.
31. M. T. Khan and A. E. Martell, Metal ion and metal chelate catalyzed oxidation of ascorbic acid by molecular oxygen. I. Cupric and ferric ion catalyzed oxidation, *Journal of the American Chemical Society*, 1967, **89**, 4176-4185.
32. P. M. Wood, The potential diagram for oxygen at pH 7, *Biochemical Journal*, 1988, **253**, 287.
33. I. H. Segel, *Biochemical calculations: how to solve mathematical problems in general biochemistry*, John Wiley & Sons, 1991.
34. H. Sun, G. Xie, D. He and L. Zhang, Ascorbic acid promoted magnetite Fenton degradation of



alachlor: Mechanistic insights and kinetic modeling, *Applied Catalysis B: Environmental*, 2020, **267**, 118383. View Article Online  
DOI: 10.1039/D5VA00420A

35. D. H. Truong, T. C. Ngo, N. T. A. Nhung, D. T. Quang, T. L. A. Nguyen, D. Khiri, S. Taamalli, F. Louis, A. El Bakali and D. Q. Dao, New insights into the competition between antioxidant activities and pro-oxidant risks of rosmarinic acid, *RSC advances*, 2022, **12**, 1499-1514.
36. W. Stumm and J. J. Morgan, *Aquatic chemistry: chemical equilibria and rates in natural waters*, John Wiley & Sons, 2013.
37. C. A. Juan, J. M. Pérez de la Lastra, F. J. Plou and E. Pérez-Lebeña, The chemistry of reactive oxygen species (ROS) revisited: outlining their role in biological macromolecules (DNA, lipids and proteins) and induced pathologies, *International journal of molecular sciences*, 2021, **22**, 4642.
38. W. Bors and G. Buettner, *The vitamin C radical and its reactions*, 1997.
39. Y.-J. Tu, D. Njus and H. B. Schlegel, A theoretical study of ascorbic acid oxidation and HOO/O<sub>2</sub>- radical scavenging, *Organic & biomolecular chemistry*, 2017, **15**, 4417-4431.
40. Z. Wang, J. Jiang, S. Pang, Y. Zhou, C. Guan, Y. Gao, J. Li, Y. Yang, W. Qiu and C. Jiang, Is sulfate radical really generated from peroxydisulfate activated by iron (II) for environmental decontamination?, *Environmental Science & Technology*, 2018, **52**, 11276-11284.
41. G. Tachiev, J. Roth and A. Bowers, Kinetics of hydrogen peroxide decomposition with complexed and “free” iron catalysts, *International Journal of Chemical Kinetics*, 2000, **32**, 24-35.
42. P. Refait, C. Bon, L. Simon, G. Bourrie, F. Trolard, J. Bessière and J.-M. Génin, Chemical composition and Gibbs standard free energy of formation of Fe (II)-Fe (III) hydroxysulphate green rust and Fe (II) hydroxide, *Clay Minerals*, 1999, **34**, 499-510.
43. N. Bazhin, Standard and transformed values of gibbs energy formation for some radicals and ions involved in biochemical reactions, *Archives of Biochemistry and Biophysics*, 2020, **686**, 108282.
44. V. A. Timoshnikov, T. V. Kobzeva, N. E. Polyakov and G. J. Kontoghiorghes, Redox interactions of vitamin C and iron: Inhibition of the pro-oxidant activity by deferiprone, *International journal of molecular sciences*, 2020, **21**, 3967.
45. L. Deguillaume, M. Leriche and N. Chaumerliac, Impact of radical versus non-radical pathway in the Fenton chemistry on the iron redox cycle in clouds, *Chemosphere*, 2005, **60**, 718-724.
46. B. HALLIWELL, *Ascorbic acid and the illuminated chloroplast*, in: *Ascorbic acid: Chemistry*,



*metabolism, and uses*, ACS Publications, 1982.

View Article Online  
DOI: 10.1039/D5VA00420A

47. M. A. SIDDIQI and E. BOTHE, Single- and double-strand break formation in DNA irradiated in aqueous solution: dependence on dose and OH radical scavenger concentration, *Radiation Research*, 1987, **112**, 449-463.
48. R. Herscu-Kluska, A. Masarwa, M. Saphier, H. Cohen and D. Meyerstein, Mechanism of the reaction of radicals with peroxides and dimethyl sulfoxide in aqueous solution, *Chemistry–A European Journal*, 2008, **14**, 5880-5889.
49. J. L. Wilmoth, J. K. Schaefer, D. R. Schlesinger, S. W. Roth, P. G. Hatcher, J. K. Shoemaker and X. Zhang, The role of oxygen in stimulating methane production in wetlands, *Global Change Biology*, 2021, **27**, 5831-5847.
50. S. Kihara, D. A. Hartzler and S. Savikhin, Oxygen concentration inside a functioning photosynthetic cell, *Biophysical journal*, 2014, **106**, 1882-1889.
51. A. Sauer, H. Cohen and D. Meyerstein, The methyl (cyclam) nickel (III) dication in aqueous solutions: determination of the equilibrium constant of homolysis, kinetics of oxygen insertion, and methyl transfer to aquated chromium (2+), *Inorganic Chemistry*, 1988, **27**, 4578-4581.
52. C. Tang and S.-Z. Qiao, How to explore ambient electrocatalytic nitrogen reduction reliably and insightfully, *Chemical Society Reviews*, 2019, **48**, 3166-3180.
53. S. Matera, W. F. Schneider, A. Heyden and A. Savara, Progress in accurate chemical kinetic modeling, simulations, and parameter estimation for heterogeneous catalysis, *Acs Catalysis*, 2019, **9**, 6624-6647.
54. S. Sharma, Quantum algorithms for simulation of quantum chemistry problems by quantum computers: an appraisal, *Foundations of Chemistry*, 2022, **24**, 263-276.
55. M. Reiher, N. Wiebe, K. M. Svore, D. Wecker and M. Troyer, Elucidating reaction mechanisms on quantum computers, *Proceedings of the national academy of sciences*, 2017, **114**, 7555-7560.
56. J. D. Whitfield, J. Biamonte and A. Aspuru-Guzik, Simulation of electronic structure Hamiltonians using quantum computers, *Molecular Physics*, 2011, **109**, 735-750.
57. A. W. Harrow, A. Hassidim and S. Lloyd, Quantum algorithm for linear systems of equations, *Physical review letters*, 2009, **103**, 150502.
58. V. V. Nenonen, R. Kaegi, S. J. Hug, J. Luster, J. Göttlicher, S. Mangold, L. H. Winkel and A. Voegelin, Effects of organic ligands, phosphate and Ca on the structure and composition of Fe (III)-precipitates formed by Fe (II) oxidation at near-neutral pH, *Environmental Science: Processes & Impacts*, 2025, **27**, 2479-2506.



59. U. Azad and H. Singh, Quantum chemistry calculations using energy derivatives on quantum computers, *Chemical Physics*, 2022, **558**, 111506. [View Article Online](#)  
DOI: 10.1039/D5VA00420A
60. S.-C. Liu, X.-R. Zhu, D.-Y. Liu and D.-C. Fang, DFT calculations in solution systems: solvation energy, dispersion energy and entropy, *Physical Chemistry Chemical Physics*, 2023, **25**, 913-931.
61. J. Krzystek, J. England, K. Ray, A. Ozarowski, D. Smirnov, L. Que Jr and J. Telsler, Determination by high-frequency and-field EPR of zero-field splitting in iron (IV) oxo complexes: Implications for intermediates in nonheme iron enzymes, *Inorganic chemistry*, 2008, **47**, 3483-3485.
62. B. F. Staley, F. L. de los Reyes III and M. A. Barlaz, Effect of spatial differences in microbial activity, pH, and substrate levels on methanogenesis initiation in refuse, *Applied and environmental microbiology*, 2011, **77**, 2381-2391.
63. M. Flinck, S. Kramer and S. Pedersen, Roles of pH in control of cell proliferation, *Acta Physiologica*, 2018, **223**, e13068.
64. G. Pelaz, D. Carrillo-Pena, A. Morán and A. Escapa, Microbial electromethanogenesis for energy storage: Influence of acidic pH on process performance, *Journal of Energy Storage*, 2024, **75**, 109685.



## Data Availability Statement

View Article Online  
DOI: 10.1039/D5VA00420A

All datasets used in this study are derived from previously published papers, which are properly referenced and cited within the manuscript. No new datasets were generated or analysed during this research.

